







RESEARCH ARTICLE | APRIL 13 2023

## Transitional criterion and hysteresis of multiple shock–shock interference

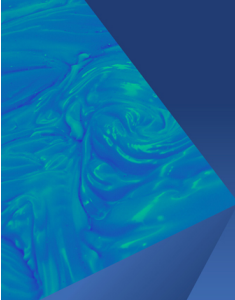
Special Collection: [Shock Waves](#)

Lin Mingyue (林明月) ; Yang Fan (杨帆) ; Hu Zongmin (胡宗民)  ; Wang Chun (王春) ;  
Jiang Zonglin (姜宗林) 



*Physics of Fluids* 35, 046110 (2023)


<https://doi.org/10.1063/5.0146200>



## Physics of Fluids

Special Topic:  
John Michael Dealy (1937-2024): Celebrating His Life  
Guest Editors: Alan Jeffrey Giacomini and Savvas G. Hatzikiriakos

[Submit Today!](#)



# Transitional criterion and hysteresis of multiple shock–shock interference

Cite as: Phys. Fluids **35**, 046110 (2023); doi: 10.1063/5.0146200

Submitted: 11 February 2023 · Accepted: 28 March 2023 ·

Published Online: 13 April 2023



View Online



Export Citation



CrossMark

Mingyue Lin (林明月),<sup>1,2</sup> Fan Yang (杨帆),<sup>1,2</sup> Zongmin Hu (胡宗民),<sup>1,2,a)</sup> Chun Wang (王春),<sup>1,2</sup>   
and Zonglin Jiang (姜宗林)<sup>1,2</sup>

## AFFILIATIONS

<sup>1</sup>State Key Laboratory of High-temperature Gas Dynamics, Chinese Academy of Sciences, Beijing 100190, People's Republic of China

<sup>2</sup>School of Engineering Science, University of Chinese Academy of Sciences, Beijing 100049, People's Republic of China

Note: This paper is part of the special topic, Shock Waves.

<sup>a)</sup> Author to whom correspondence should be addressed: [huzm@imech.ac.cn](mailto:huzm@imech.ac.cn)

## ABSTRACT

In this study, oblique-shock/bow-shock interference is theoretically and numerically studied with two incident shock waves. The transition criteria between the two modes of multiple shock–shock interference, i.e., the concomitant-jet (CJ) and dual-jet (DJ) modes, are given. The oblique shock relationship and shock polar analysis are utilized to obtain the analytical solution of the transition condition. The theoretical results indicate the existence of a dual solution interval (DSI) that widens with increasing Mach number and narrows with increasing deflection angle induced by the first incident shock wave. The DSI obtained by numerical simulation is considerably narrower than that theoretically predicted due to the advanced CJ→DJ and DJ→CJ transitions. The analysis reveals that the transitions are advanced due to the downstream disturbance and secondary waves in the flow field.

Published under an exclusive license by AIP Publishing. <https://doi.org/10.1063/5.0146200>

## NOMENCLATURE

$D$	diameter of the cylinder
$Ir$	dimensionless position parameter of the incident shock wave
$k$	flow parameters in region ( $k$ )
$M_u$	upstream Mach number
$Ma$	Mach number
$Ma_\infty$	freestream Mach number
$p$	pressure
$p_0$	stagnation pressure
$R$	radius of the cylinder
$T_w$	wall temperature
$x, y$	horizontal and vertical coordinates
$\beta$	shock angle
$\beta_{\max}$	maximum shock angle
$\gamma$	specific heats ratio equals 1.4
$\Delta t$	flow characteristics time
$\theta$	flow deflection angle
$\theta_i^{Det}, \theta_i^{St}, \theta_i^{vN}$	critical angle of $\theta_i$ for detachment condition, stationary condition, and von Neumann condition, respectively. $i = 1, 2$ .

$\theta_{\max}$	maximum flow deflection angle
$\xi$	pressure ratio
$\phi$	turning angle of the compression ramp

## I. INTRODUCTION

Hysteresis is a general property of multi-stable systems that depends on their evolutionary history.<sup>1</sup> The hysteresis in steady shock wave reflection is best known, but it has been investigated through a long and tortuous process. In the late 1870s, Ernst Mach<sup>2</sup> experimentally recorded two different shock-wave reflections, i.e., regular reflection (RR) and Mach reflection (MR), and laid the foundations for the generous studies on shock wave reflection. Von Neumann<sup>3</sup> first introduced the two critical conditions between the RR↔MR transition: the detachment and von Neumann conditions. Beyond the detachment condition, the RR configuration is theoretically impossible, and below the von Neumann condition, the MR configuration no longer exists. Hornung *et al.*<sup>4</sup> hypothesized that hysteresis could exist in the RR↔MR transition. However, both Henderson and Lozzi<sup>5</sup> and Hornung and Robinson<sup>6</sup> did not observe hysteresis in their experiments. They concluded that the RR wave configuration is unstable in the dual solution interval (DSI). Chpoun *et al.*<sup>7</sup> were the first to

experimentally record the stable RR configuration inside DSI and a wedge-angle-induced hysteresis in the RR $\leftrightarrow$ MR transition. Then, Vuillon *et al.*<sup>8</sup> numerically obtained both stable RR and MR configurations for the same Mach numbers and wedge angles. The above-mentioned experimental and numerical studies kindled the interest of researchers on the hysteresis in the RR $\leftrightarrow$ MR transition. Ben-Dor *et al.*<sup>9</sup> and Hornung<sup>10</sup> reviewed the literature related to this subject. The persistent interest of the scientific community on hysteresis is due to not only its academic background but also its important impact on flight performance at supersonic speeds.<sup>9</sup> Consequently, many researchers<sup>11–14</sup> have discussed hysteresis loops in geometries that resemble the geometries of components of flight vehicles.

Shock–shock interference<sup>15–19</sup> (SSI) of a single oblique shock wave intersecting with a bow shock has been extensively studied in the past 50 years since Edney's pioneering work.<sup>20</sup> Type IV SSI has received significant attention because it produces severe aero-heating<sup>15</sup> and is rich in complex flows.<sup>21</sup> This configuration can be commonly found in the internal and external flow fields of hypersonic vehicles. However, under certain circumstances, a considerably more complex phenomenon may arise wherein multiple shock waves intersect a bow shock at bordering locations, which is called multiple SSI (MSSI). MSSI can be observed when compression shock waves of multi-stage compression surfaces fail to converge at the inlet entrance or when an unexpected shock wave is generated due to the separation of the boundary layer from the compression corner. MSSI can also be observed at the leading edge of wings or fins when extra shocks are generated because of the separation of the boundary layer of the fuselage. In addition to the inherent flow involved in classical SSI, MSSI comprises complicated and interesting flow physics and is worthy of further study.

The interference between multiple oblique shock waves, notably the shock interference for double-wedge<sup>22–24</sup>/cone<sup>25,26</sup> configurations, has received some attention. Olejniczak *et al.*<sup>27</sup> numerically represented the inviscid shock interactions for double-wedge geometries and identified the transition criteria between the various interactions. Hu *et al.*<sup>28</sup> numerically confirmed the existence of an overall MR (oMR) configuration with double inverse MR (InMR) patterns for a double-wedge geometry. They proposed a geometric criterion for the transition between RR and MR for a double-wedge geometry.<sup>29</sup> Considering nonequilibrium high-temperature gas effects, Xiong *et al.*<sup>30</sup> examined the transition of type V SSI for a double-wedge geometry. In recent years, numerous studies<sup>31–33</sup> have focused on the influence of the real-gas effect on interference characteristics over double-wedge and double-cone configurations. Guan *et al.*<sup>34</sup> stated that shock reflection for the double-wedge configuration is usually studied without considering a reflecting surface. They placed a reflecting surface at the intersecting point of two incident shock waves and studied the shock reflection with double incident shock waves.<sup>35,36</sup> According to Guan *et al.*, three types of reflections may occur when two incident shock waves are reflected at the same point: RR, pre-MR, and post-MR. Analogously, MSSI can be obtained by replacing the reflecting surface with a bow shock wave.

To date, few studies have been conducted on MSSI. Wieting<sup>37</sup> was the first to conduct detailed experiments on the shock interactions of two incident oblique shock waves. Two types of MSSI patterns were observed: concomitant-jet (CJ) and dual-jet (DJ) patterns. The CJ pattern constitutes two supersonic jets separated from each other by a

shear layer, while the DJ pattern constitutes two jets separated by a subsonic region. This experiment was numerically repeated by Hsu and Ijaz,<sup>38</sup> who determined that the pattern of DJ identified in the experiment exists only temporarily and eventually transforms into the CJ pattern. They inferred that the CJ pattern is the only possible quasi-steady-state solution. Since then, no further studies have been conducted on these two patterns of MSSIs, except the study on the distribution characteristics of surface heat transfer by Jiang *et al.*<sup>39</sup> and verification for the numerical scheme by Hsieh *et al.*<sup>40</sup>

This study aims to clarify three issues. The first is the critical condition for DJ interference, i.e., verifying whether the DJ mode is stable. The second is to numerically confirm the DJ pattern, since the numerical results of the steady DJ pattern have not been reported in the literature. The third is to analyze the transition criterion between the two patterns of MSSI and determine whether hysteresis exists.

This study attempts to investigate the aforementioned three issues within the context of the inviscid flow of a perfect gas. The transition criteria of MSSI are established through shock polar analysis. Numerical simulations are performed to determine the detailed flow structures and verify the hysteresis. This paper is organized as follows. In Sec. II, the conditions to obtain CJ and DJ patterns in MSSI are theoretically derived. In Sec. III, numerical simulations are presented to support the theoretical results and depict more detailed flow structures for MSSI. Moreover, discrepancies between the theoretical and numerical results are analyzed. Conclusions are presented in Sec. IV.

## II. THEORETICAL ANALYSIS

The geometric description of MSSI is provided in Sec. II A. Criteria, assumptions, and shock theory are given in Sec. II B. The sufficient condition for CJ $\rightarrow$ DJ transition and the necessary condition for DJ $\rightarrow$ CJ transition are presented in Sec. II C. The theoretically obtained DSI is shown in Sec. II D.

### A. Geometry description

Figure 1 displays the geometric configuration of the MSSI studied herein. The first incident shock wave  $K_1A$  intersects with the strong portion of the bow shock wave and induces type IV SSI. The second incident shock  $K_2I$  intersects with the transmitted shock of  $K_1A$ , i.e., AI, and completes the MSSI. MSSI in other shapes can be produced by changing the intersection positions of the two incident shock waves. For example,  $K_1A$  is incident on the supersonic portion of the bow shock wave or  $K_2I$  intersects with the bow shock segment BC. Among all the possible interferences, the configuration shown in Fig. 1 is particularly interesting and needs to be studied. The MSSI transitions determined by Hsu and Ijaz<sup>38</sup> also occur within this configuration.

The transition criterion of MSSI is based on the types of shock reflection at the intersection point. As shown in Fig. 2, RR [Fig. 2(a)] and MR [Fig. 2(b)] can occur at point I, corresponding to the CJ and DJ patterns of MSSI, respectively. The transition of MSSI is not substantially different from that of an asymmetric shock reflection but is more complex. In this case, one incident shock wave is replaced by the transmitted shock wave of MR (AI in Fig. 1), the parameters of which are unknown and need to be solved. Another issue that needs to be clarified is whether the transmitted shock wave AI is strong enough to generate MR at point I.

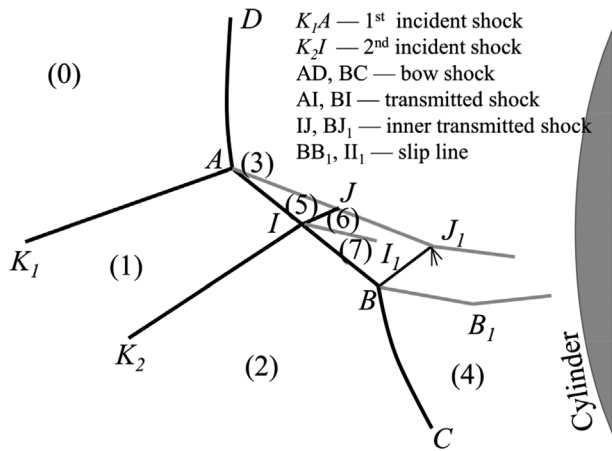


FIG. 1. Illustration of the MSSSI configuration with the second incident shock  $K_2I$  intersecting with the transmitted shock  $AI$ .

**B. Assumptions and shock polar**

Next, the transition condition is theoretically solved. The following two assumptions are made. First,  $K_2I$  initially intersects with  $AI$ . Second,  $AI$  is assumed to be straight, that is, the influence of secondary waves is ignored. Classical shock relationships for perfect gas are used herein. As shown in Figs. 1 and 2, the overall flow field is divided into several flow regions. The flow is uniform in regions (0)–(2) and considered uniform in infinitely small regions near the intersection points of shock waves in regions (3)–(12). The subscript  $k$  is used to denote the flow parameters in the region ( $k$ ). Pressure–deflection ( $p$ – $\theta$ ) shock polars are utilized to illustrate the derivation of the MSSSI transition criteria.  $\Gamma(k)$  denotes the shock polar, along which the locus of all the flow states downstream of any shock wave generated in region ( $k$ ) is present. The entire region behind a planar shock wave can be represented by a single point on the ( $p$ – $\theta$ ) diagram. The flow deflection angle  $\theta$  and pressure ratio  $\xi$  across an oblique shock wave can be obtained by the upstream Mach number  $M$  and shock angle  $\beta$ , respectively, which are given as

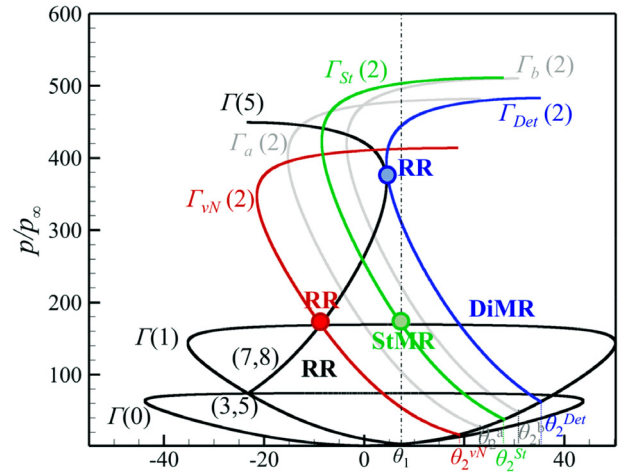


FIG. 3. Critical pressure–deflection shock polars for MSSSI at  $M_0 = 8.0$  and  $\theta_1 < \theta_1^{St}$ .

$$\theta = \theta(\gamma, M, \beta) = \arctan \left\{ \frac{2 \cot \beta (M^2 \sin^2 \beta - 1)}{M^2 (\cos 2\beta + \gamma) + 2} \right\}, \quad (1)$$

$$\xi = \xi(\gamma, M, \beta) = 1 + \frac{2\gamma}{\gamma + 1} (M^2 \sin^2 \beta - 1). \quad (2)$$

Here,  $\gamma$  denotes the ratio of specific heat, which is 1.4 in this study. The flow deflection angle is assumed to be positive if it deflects toward the shock wave. The transition criteria are displayed by the shock polar diagram (Fig. 3). Polar  $\Gamma(0)$  is the locus of the flow state downstream of the incoming flow (0). Given that the flow deflection angle across  $K_1A$  is  $\theta_1$ , the flow parameters in region (1) lie at the point  $(\theta_1, p_1/p_\infty)$ . Polar  $\Gamma(1)$  is the locus of the flow states connected to the state  $(\theta_1, p_1/p_\infty)$  by any shock wave, which may be a weak solution, such as oblique shock  $K_2I$ , or a strong solution, such as a Mach stem  $I'$  [Fig. 2(b)]. An intersection exists between polars  $\Gamma(0)$  and  $\Gamma(1)$ . This intersection yields two flow states: state (3) downstream of the Mach stem (denoted as  $AD$  in Fig. 1) and state (5) downstream of the transmitted shock (denoted as  $AI$  in Fig. 1). Thus, the intersection of polar  $\Gamma(0)$  and  $\Gamma(1)$  represents the upper triple point formed by the

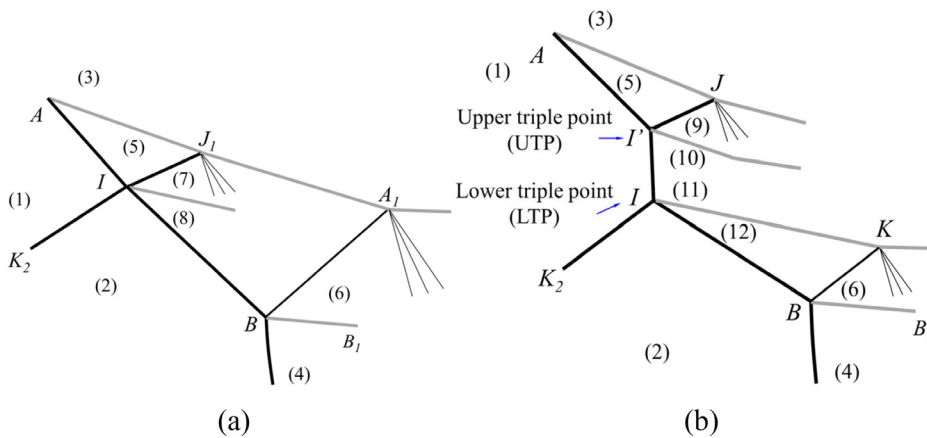


FIG. 2. Types of shock interference/reflection at point I: (a) type I, RR and (b) type II, MR.

intersection of  $K_1A$  and the bow shock wave  $AD$  (Fig. 1). Starting from state (5), polar  $\Gamma(5)$  is the locus of the flow states connected to state (5) by any shock, which may be a weak solution, such as transmitted shock  $[IJ$  in Fig. 2(a)], or a strong solution, such as a Mach stem  $[I\Gamma$  in Fig. 2(b)]. Polar  $\Gamma(5)$  intersects with the upper part of polar  $\Gamma(1)$ , producing another triple point, which is denoted as  $\Gamma$  in Fig. 2(b). The flow parameters in regions (1), (3), and (5) can be determined by  $M_0$  and  $\theta_1$ .

C. Transition criterion

Next, the necessary condition for  $DJ \rightarrow CJ$  transition is considered, i.e., the von Neumann condition  $\theta_2^{vN}(M_0, \theta_1)$  to produce  $RR$  at point  $I$  [Fig. 2(a)]. The von Neumann condition is satisfied when the pressure downstream of an infinitely small strong shock wave  $[I\Gamma$  in Fig. 2(b) for reference] is balanced by the pressure in regions (7) and (8),

$$p_7 = p_8 = p_{10/11}. \tag{3}$$

In the shock polar diagram (Fig. 3), state (10) is represented by the intersection point of polars  $\Gamma(1)$  and  $\Gamma(5)$ . Hence, Eq. (3) is satisfied when  $\Gamma(2)$  passes through the intersection point between polars  $\Gamma(1)$  and  $\Gamma(5)$ , as shown by  $\Gamma_{vN}(2)$  in Fig. 3.

The sufficient condition for  $CJ \rightarrow DJ$  transition, i.e., the detachment condition  $\theta_2^{Det}(M_0, \theta_1)$  to produce  $MR$  at point  $I$  [Fig. 2(b)], is realized when the shock polar  $\Gamma(2)$  is tangent to polar  $\Gamma(5)$ , as represented by  $\Gamma_{Det}(2)$  in Fig. 3. An intermediate angle  $\theta_2^{St}(M_0, \theta_1)$  exists between  $\theta_2^{vN}(M_0, \theta_1)$  and  $\theta_2^{Det}(M_0, \theta_1)$ , wherein the  $SL$  stemming from  $I$  is parallel to the flow in the region (1). In other words, the flows of regions (1), (11), and (12) are in the same direction. The intersection of  $\Gamma(1)$  and  $\Gamma_{St}(2)$  indicates a stationary  $MR$  ( $StMR$ ).  $SL$  is denoted as a parallel slip line of the lower triple point: lower parallel slip line ( $LpSL$ ). When  $\theta_2^{vN} < \theta_2 < \theta_2^{St}$ , the polar  $\Gamma_a(2)$  intersects the upper-left part of  $\Gamma(1)$  and signifies an  $InMR$ . In this case, the lower slip line deflects downward, which is denoted as the downward slip line of the lower triple point: lower downward slip line ( $LdSL$ ). When  $\theta_2^{St} < \theta_2 < \theta_2^{Det}$ , the polar  $\Gamma_b(2)$  intersects the upper-right part of  $\Gamma(1)$  and signifies a direct  $MR$  ( $DiMR$ ). The slip line stemming from  $I$  deflects upward and is denoted as the upward slip line of the lower triple point: lower upward slip line ( $LuSL$ ).

Moreover, a critical angle  $\theta_1^{St}$  exists; in this case, the slip line originating from the triple point  $A$  is parallel to the flow in region (1). Figure 3 illustrates the shock polar analysis for a fixed  $\theta_1$  when  $\theta_1 < \theta_1^{St}$ . Figure 4 displays the schematic of the shock polar analysis when  $\theta_1 > \theta_1^{St}$ . Since the shock polar system is similar, the analysis for it is omitted here.

D. Dual solution interval

The theoretical criteria sketched in Figs. 3 and 4, i.e.,  $\theta_1^{St}$ ,  $\theta_2^{vN}$ ,  $\theta_2^{St}$ , and  $\theta_2^{Det}$ , are plotted in the  $(\theta_1, \theta_2)$  plane for  $M_\infty = 8$  in Fig. 5. Figure 5 shows that the line of von Neumann criteria is well below that of the detachment criteria, indicating the existence of  $DSI$ . The line of stationary criterion divides the  $MR$  domain into two parts in each dimension of Fig. 5. On one side of  $\theta_1^{St}$  or  $\theta_2^{St}$ , the  $MR$  is direct, i.e.,  $DiMR$ , and is inverse on the other side, i.e.,  $InMR$ . On the criteria line itself, the  $MR$  is stationary, i.e.,  $StMR$ . Thus, the  $DSI$  shown in Fig. 5 is divided into three parts. One part is labeled “4 + 1,” whose overall wave configuration can be either  $CJ$  or  $DJ$ .  $DJ$  comprises a downward

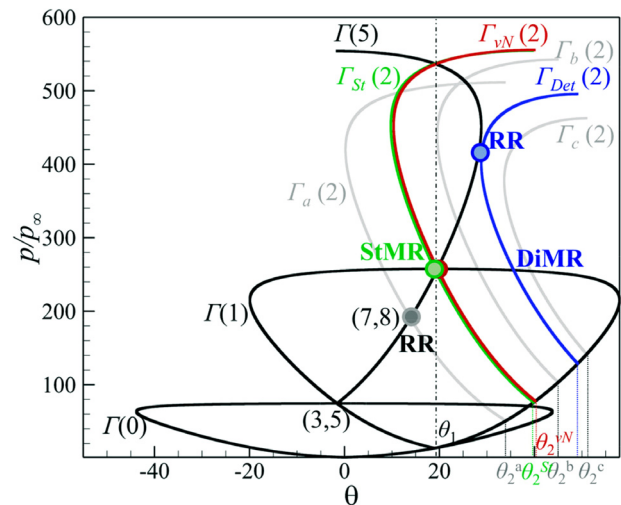


FIG. 4. Critical pressure–deflection shock polars for MSSl at  $M_0 = 8.0$  and  $\theta_1 > \theta_1^{St}$ .

slip line of the upper triple point (upper downward slip line;  $UdSL$ ) and a  $LdSL$ , i.e.,  $DJ$  [ $UdSL + LdSL$ ]. The overall wave configuration of another part, which is labeled as “4 + 2” in Fig. 5, can also be either  $CJ$  or  $DJ$ . In this case,  $DJ$  comprises an  $UdSL$  and a  $LuSL$ , i.e.,  $DJ$  [ $UdSL + LuSL$ ]. The last part, which is labeled as “4 + 3” in Fig. 5, is composed of either  $CJ$  or  $DJ$ , and  $DJ$  comprises one upper upward slip line ( $UuSL$ ) and one  $LuSL$ , i.e.,  $DJ$  [ $UuSL + LuSL$ ]. Figure 5 shows that depending on whether  $\theta_1$  is smaller or larger than  $\theta_1^{St}$ , two different sequences of transitions of interference configurations occur during the process of first increasing  $\theta_2$  and then decreasing it to its initial value.

Figure 6 displays the sequence of shock polar solutions for  $\theta_1 = 7.5^\circ < \theta_1^{St}$ . The theoretical results suggest the following wave

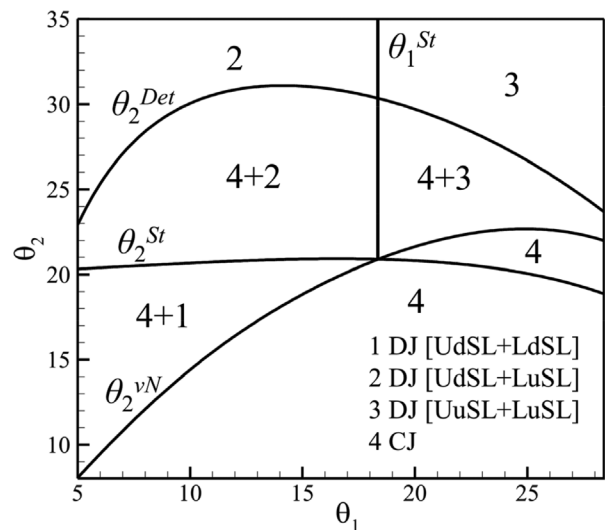


FIG. 5. Transition criteria for MSSl demonstrating  $DSI$  in the  $(\theta_1 - \theta_2)$  plane for  $M_\infty = 8.0$ .

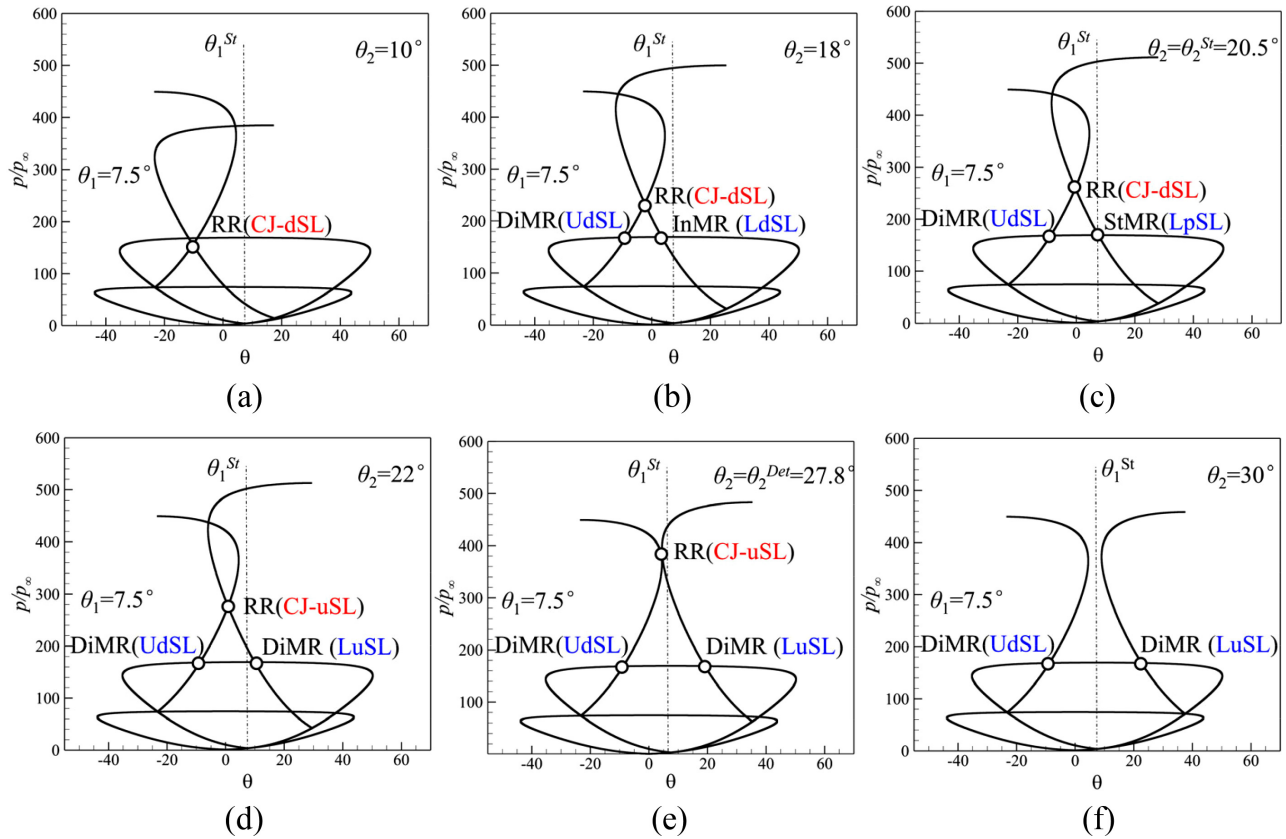


FIG. 6. Shock polar solutions illustrating the hysteresis loop for  $M_0 = 8.0$ ,  $\theta_1 = 7.5^\circ < \theta_1^{St}$ ,  $\theta_2 = 10^\circ$  (a),  $18^\circ$  (b),  $20.5^\circ$  (c),  $22^\circ$  (d),  $27.8^\circ$  (e), and  $30^\circ$  (f).

configuration sequence. The sequence commences with a CJ at  $\theta_2 = 10^\circ$  [Fig. 6(a)]. In this case, the only slip line originating from the intersecting point I [Fig. 2(a)] deflects downward relative to the free-stream, which is labeled as the downward slip line (dSL) in Fig. 6(a). The CJ configuration is maintained with increasing  $\theta_2$  [Figs. 6(a)–6(d)] until the detachment criterion  $\theta_2^{Det}$  [Fig. 6(e)]. At this point, the CJ pattern translates into DJ [UdSL + LuSL], i.e., the upper slip line deflects downward and the lower slip line deflects upward in the DJ pattern. On the reverse path, DJ [UdSL + LuSL] [Figs. 6(d)–6(f)] is maintained with decreasing  $\theta_2$  until the stationary criterion  $\theta_2^{St}$ . The wave configuration changes to DJ [UdSL + LpSL] exactly when  $\theta_2 = \theta_2^{St}$  [Fig. 6(c)]. In this case, the lower jet is parallel to the flow in region (1) (Fig. 1). Then, it translates into DJ [UdSL + LdSL] and persists until the von Neumann criterion:  $\theta_2^{vN}$ . At this point, DJ changes back to CJ. The sequence for  $\theta_1 < \theta_1^{St}$  can be written as follows:

$$CJ \xrightarrow{\text{at } \theta_2^{Det}} DJ[UdSL + LuSL] \xrightarrow{\text{on } \theta_2^{St}} DJ[UdSL + LpSL] \xrightarrow{\text{at } \theta_2^{St}} DJ[UdSL + LdSL] \xrightarrow{\text{at } \theta_2^{St}} CJ.$$

Figure 7 displays the shock polar solutions of the sequence for  $\theta_1 = 19^\circ > \theta_1^{St}$ , and the following wave configurations are encountered. The sequence starts with CJ and CJ is maintained [Figs. 7(a)–7(e)] until the detachment criterion  $\theta_2^{Det}$  [Fig. 7(e)]. At  $\theta_2^{Det}$ , CJ translates

into DJ [UuSL + LuSL], i.e., a DJ configuration comprising one UuSL and one LuSL. On the reverse path, DJ [UuSL + LuSL] is maintained until the von Neumann transition  $\theta_2^{vN}$  [Fig. 7(c)]. At this point, DJ reverts to CJ. This sequence is written as follows:

$$CJ \xrightarrow{\text{at } \theta_2^{Det}} DJ[UuSL + LuSL] \xrightarrow{\text{at } \theta_2^{vN}} CJ.$$

Figure 8 depicts the influence of  $\theta_1$  on DSI. The figure denotes that with increasing  $\theta_1$ , the detachment condition is elevated less than the von Neumann condition and the DSI becomes narrower.

### III. NUMERICAL VERIFICATION

Inviscid numerical simulations are performed to verify the theoretical findings. The numerical method is introduced and verified in Secs. III A and III B. Section III C presents the numerical results of the two different sequences of wave configurations presented in Sec. II D. The possible reasons for the confusing transition of the CJ mode to DJ mode observed by Hsu and Ijaz<sup>38</sup> are discussed in Sec. III D.

#### A. Governing equations and numerical algorithm

Two-dimensional compressible Euler equations are numerically solved to simulate MSS. The convection terms of the governing equations are discretized with a second-order total variation diminishing (TVD) method. An approximate Riemann solver called Harten–Lax–van

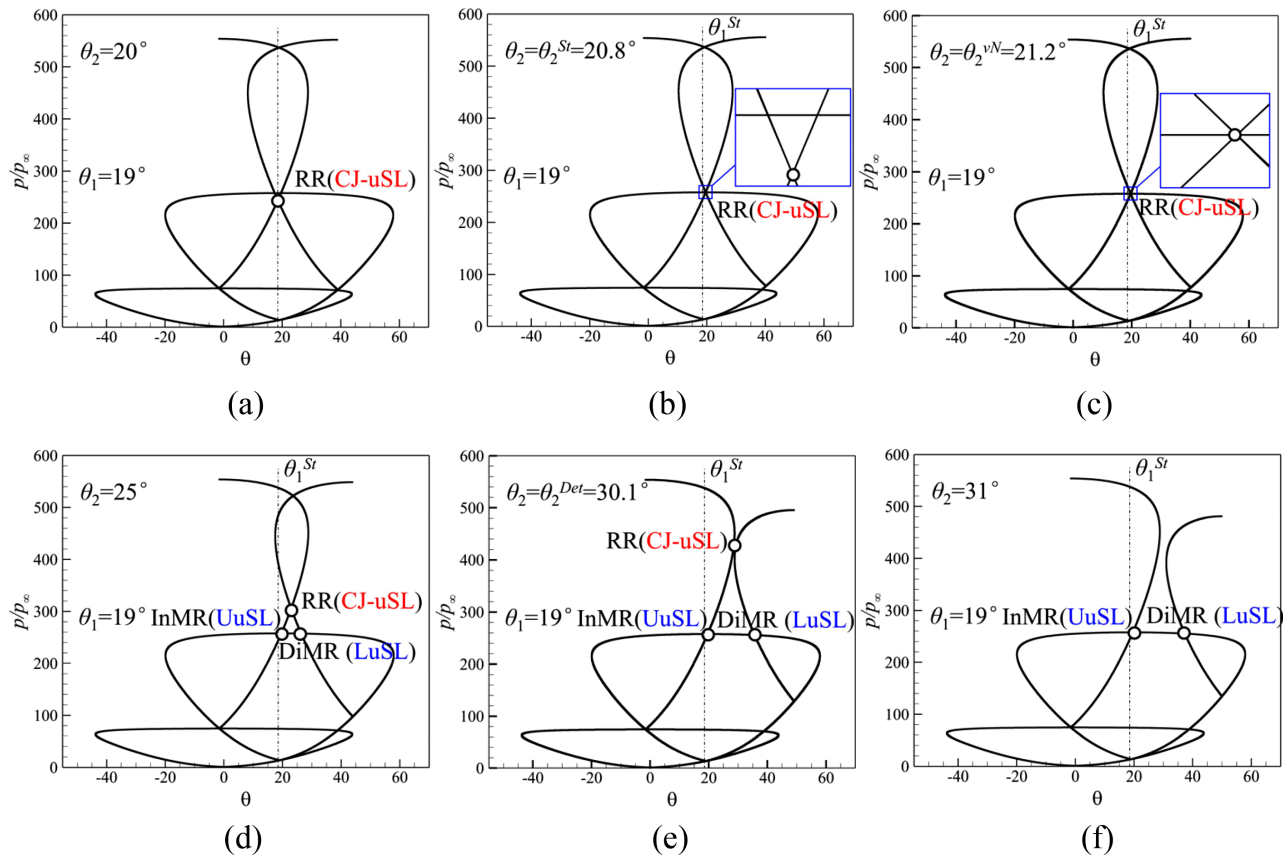


FIG. 7. Shock polar solutions illustrating the hysteresis loop for  $M_0 = 8.0$ ,  $\theta_1 = 19^\circ > \theta_1^{St}$ ,  $\theta_2 = 20^\circ$  (a),  $20.8^\circ$  (b),  $21.2^\circ$  (c),  $25^\circ$  (d),  $30.1^\circ$  (e), and  $31^\circ$  (f).

Leer contact is used to define the interface fluxes. The minmod limiter is employed to suppress the spurious oscillations near the discontinuities. Time integration is performed using a second-order fully implicit scheme. This computational code has been used and validated in Peng *et al.*,<sup>41,42</sup>

Zhang *et al.*,<sup>43</sup> and Lu *et al.*,<sup>44</sup> showing excellent performance in solving shock interactions. Turbulence, real gas effect, and unsteadiness are not considered herein.

**B. Method validation**

The first detailed experiments of MSSI conducted by Wieting<sup>37</sup> are numerically simulated to verify the reliability of the numerical method. Then, the inviscid numerical results are compared with those obtained by Hsu and Ijaz.<sup>38</sup> The numerical method used by Hsu and Ijaz is a second-order MUSCL (Monotonic Upwind Scheme for Conservation Laws)-type TVD scheme based on Roe’s approximate Riemann solver with an entropy correction. It uses a first- or second-order time discretization option in the time integration. Wieting<sup>37</sup> conducted the experiments at the Calspan University of Buffalo Research Center 48 in. Hypersonic Shock Tunnel (48 in. HST) at a nominal Mach number of 8, a total temperature of 1550 K, and a free-stream unit Reynolds number of  $4.9 \times 10^6/m$ . In the experiments, a bow shock wave was generated in front of a 7.6 cm diameter cylinder. The first incident shock wave was generated by a 7.5° shock generator wedge. An interchangeable 5° or 6° wedge was mounted downstream of the first wedge to produce the second incident shock wave. The 5° or 6° wedge and the cylinder could be translated to facilitate the acquisition of different shock interference patterns. In this study, the case of

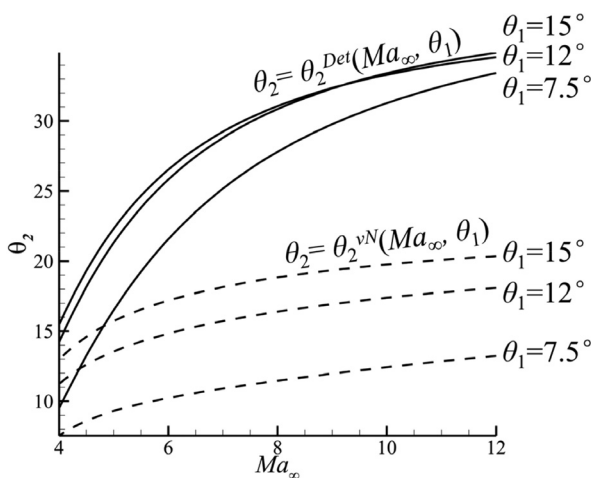


FIG. 8. Transition criteria for MSSI demonstrating the dual solution domain in the  $(Ma_\infty - \theta_2)$  plane for  $\theta_1 = 7.5^\circ, 12^\circ, \text{ and } 15^\circ$ .

Run 85 is simulated because it produced the most typical MSSI. The two deflection angles for this case are  $\theta_1 = 7.5^\circ$  and  $\theta_2 = 5^\circ$ .

Two kinds of computational domains are utilized herein. The first kind [Fig. 9(a)] is used for method validation, which contains only a portion of the front of the cylinder. This domain is consistent with the computation domain used in the simulations in Hsu and Ijaz.<sup>38</sup> The second computation domain [Fig. 9(b)] is used to verify the hysteresis. As shown in Fig. 9(b), the computational domain is bounded by inlet, outlet, and wall boundaries. The left boundary of the domain is set as the user-defined inlet, where the freestream values, post-shock values behind the first incident shock, and post-shock values behind the second incident shock are specified above and below the first and second shock impingement points, respectively. The top, right, and bottom of the computation domain are set as zero-gradient outflow. The slip boundary condition is used for the solid wall in the inviscid calculations. The main difference between these two kinds of grids is that the second computation domain [Fig. 9(b)] ensures that the flow returns to supersonic at the outlet. The reason for using this domain is provided in Sec. III D.

The comparison between the density contours calculated by Hsu and Ijaz<sup>38</sup> and the present numerical method is given in Fig. 9(a). The obvious deviation at the incident shock wave is caused by the coarse shock calculated by Hsu and Ijaz<sup>38</sup> smearing several grids. The resolution of the grid used herein is higher and the calculated shock waves are sharper than those of Hsu and Ijaz.<sup>38</sup> The distributions of nondimensionalized pressure obtained by experiments<sup>37</sup> and present inviscid computations are compared in Fig. 9(c). The comparison with the reference computational results is not provided here because Hsu and Ijaz<sup>38</sup> did not provide the results of the surface parameters for Run 85. The surface pressure  $p$  is normalized by the stagnation pressure  $p_0$  of the cylinder at the same incoming flow without shock interference. The current computational fluid dynamics results afford both the instantaneous values and arithmetic mean values obtained by the time-accurate simulation. The time step used in the simulation is less than  $1/1000$  of the flow characteristics time  $\Delta t = D/u_\infty$ , which is  $1 \times 10^{-7}$  s in this simulation. Here,  $D$  is the cylinder diameter and  $u_\infty$  is the freestream velocity. The distribution of instantaneous pressure shown in Fig. 9(c) denotes the unsteady characteristics of the flow field. The experimental measurements are averaged over the response

time of the sensor and are analogous to the numerically calculated instantaneous values. Due to the flow field oscillation, the magnitude and location of the numerically calculated peak do not exactly agree with the experimental results, but the overall trend is consistent. The flow structure is the major focus of this study. Figure 9 shows that the numerical method used herein can well reproduce the MSSI flow structures.

### C. Hysteresis phenomenon

In this section, the two different wave configuration sequences discussed in Sec. IID are validated by inviscid numerical simulations. The computational domain and boundary condition specifications are displayed in Fig. 9(b). The freestream Mach number for the cases depicted in this subsection is  $M_\infty = 8$ , and the flow deflection angle across the first incident shock wave  $\theta_1$  is  $7.5^\circ$  (Fig. 10) and  $19^\circ$  (Fig. 11). When  $\theta_1 = 7.5^\circ$ , the second flow deflection angle  $\theta_2$  varies from  $12^\circ$  to  $24^\circ$ , and when  $\theta_1 = 19^\circ$ ,  $\theta_2$  varies from  $25^\circ$  to  $26^\circ$ . The calculations are performed based on the following strategies. The first calculation of each sequence commences from a uniform incoming flow and converges to a quasi-steady state. Then, the solution of the preceding calculation is taken as the initial condition for the simulation of the new  $\theta_2$ .  $\theta_2$  is adjusted by changing the impingement position and the pre- and post-shock parameters of the incident shock waves in the settings of the user-defined inlet, given in Sec. IIIB. The relative position of the incident shock is denoted by the dimensionless position parameter  $Ir$ , which is defined as the ratio of the intercept of the incident shock to the radius of the cylinder  $R$ , i.e.,  $Ir = l/R$ . Here,  $Ir_1$  and  $Ir_2$  denote the dimensionless incident positions of the first impinging shock  $K_1A$  and the second impinging shock  $K_2I$ , respectively. The relative positions of the two incident shock waves are set as 0.15 and 0.13 herein and are kept constant throughout the sequence. The convergence of the interference flow field is impossible to realize because the flow is inherently unstable. Unsteady phenomena exist that are connected to the Kelvin–Helmholtz instability of the shear layers and oscillations of the supersonic jets. Time-accurate simulations are performed with the time step of less than  $1/1000$  of the flow characteristics time  $\Delta t = D/u_\infty$ . The solution is considered converged when the overall MSSI configuration remains unchanged or oscillates in small regions during several iteration steps.

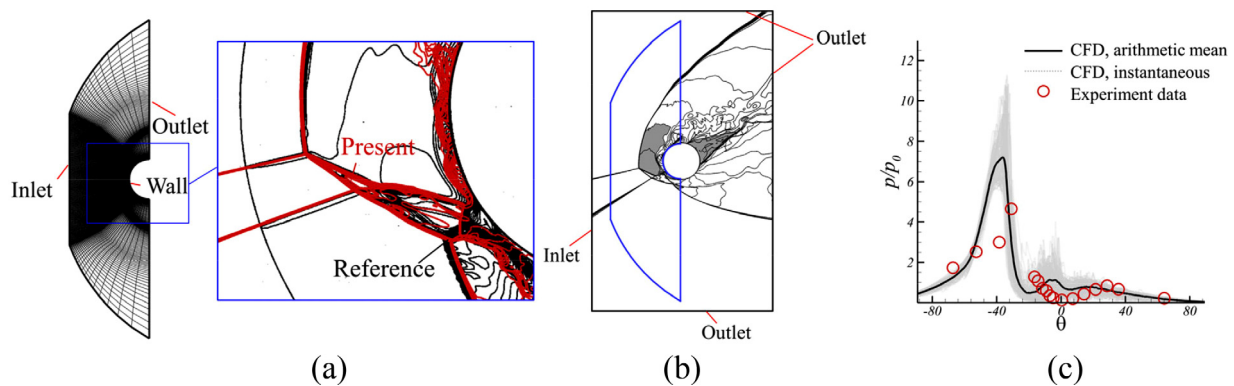
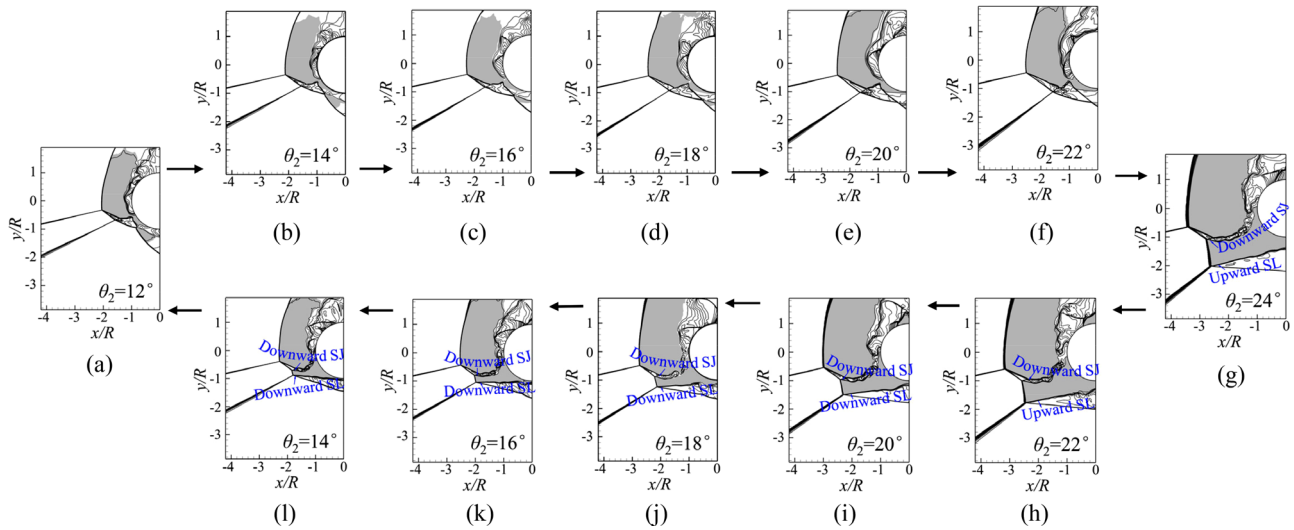


FIG. 9. Validation of the numerical method and the computation domain used for the numerical simulations. (a) Domain, grid generation, and comparison of density contour for method verification. (b) Computation domain. (c) Comparison of pressure obtained by numerical simulation and experiment.





**FIG. 10.** Numerical results with Mach contours illustrating the hysteresis loop for  $M_\infty = 8.0$ ,  $\theta_1 = 7.5^\circ$ ,  $\theta_2 = 12^\circ$  (a),  $14^\circ$  (b),  $16^\circ$  (c),  $18^\circ$  (d),  $20^\circ$  (e),  $22^\circ$  (f), and  $24^\circ$  (g) in the process of  $\theta_2$  increase and  $\theta_2 = 22^\circ$  (h),  $20^\circ$  (i),  $18^\circ$  (j),  $16^\circ$  (k), and  $14^\circ$  (l) in the process of  $\theta_2$  reduction.

Figure 10 displays the numerical results of the first sequences of wave configurations for  $M_\infty = 8.0$  and  $\theta_1 = 7.5^\circ$ , i.e.,  $\theta_1 < \theta_1^{St}$ . The flow interference structures of MSSJ are displayed by the constant Mach number lines and the subsonic regions are colored gray. The origin of the coordinates is located at the center of the cylinder and  $x$  and  $y$  are normalized by  $R$ . The vertical pairs of the figures, i.e., Figs. 10(b) and 10(l), 10(c) and 10(k), 10(d) and 10(j), 10(e) and 10(i), and 10(f) and 10(h), share the same boundary conditions but develop from different initial flow fields. Thus, the existence of hysteresis in MSSJ is verified. Since the relative positions of the two incident shock waves,  $Ir_1$  and  $Ir_2$ , are kept constant in the numerical simulations, the impingement position of the second incident shock gradually shifts downward with increasing second incident shock angle. As shown in Figs. 10(g)–10(l) and 11(b)–11(c), the lower jet exists in the form of a slip line. The classical configuration of the DJ pattern comprising two type IV supersonic jets can be obtained by shifting the relative positions of the two incident shock waves upward.

Figures 10(f) and 10(g) show that the numerical critical values for the CJ→DJ transition are between  $22^\circ$  and  $24^\circ$ , which is considerably lower than the theoretical value of  $\theta_2^{Det}$ , which is  $27.8^\circ$ . Figures 10(l) and 10(a) show that the DJ→CJ transition occurs between  $12^\circ$  and  $14^\circ$ , which is slightly higher than  $\theta_2^{vN} = 11.5^\circ$ . Thus, the DSI obtained by numerical simulation is narrower than that theoretically obtained. Numerical results of the second sequences of the wave configurations for  $M_\infty = 8.0$  and  $\theta_1 = 19^\circ$ , i.e.,  $\theta_1 > \theta_1^{St}$ , are shown in Fig. 11. In this case, the MR at triple point A can only be an InMR, with the slip line deflecting upward. Figure 11 shows that the CJ→DJ transition occurs when  $25^\circ < \theta_2 < 25.5^\circ$ , while the DJ→CJ transition occurs when  $25.5^\circ < \theta_2 < 26^\circ$ . The numerical results indicate that both the CJ→DJ and DJ→CJ transformations are dramatically advanced compared to the theoretical values, leading to the disappearance of DSI for  $M_\infty = 8.0$  and  $\theta_1 = 19^\circ$ . The CJ→DJ transition is advanced due to the occurrence of DJ at  $\theta_2 < \theta_2^{Det}$ , which is theoretically disallowed.

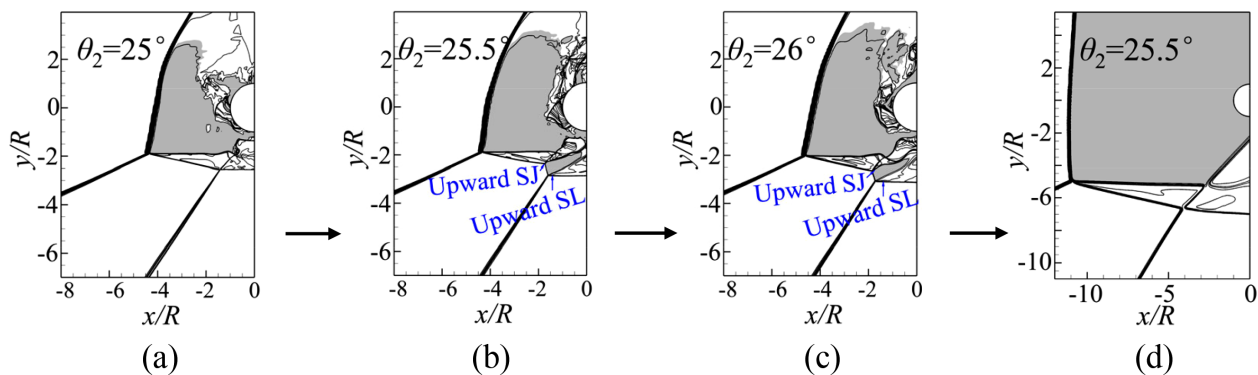


**FIG. 11.** Numerical results with Mach contours illustrating the transformation of wave structures for  $M_\infty = 8.0$ ,  $\theta_1 = 19^\circ$  and  $\theta_2 = 25^\circ$  (a),  $25.5^\circ$  (b),  $26^\circ$  (c), and  $25.5^\circ$  (d).

**TABLE I.** Comparison of the pressure ratios of different interference regions obtained by shock polar analysis (theory) and numerical calculations (simulation). The case with superscript \* indicates the DJ pattern; otherwise, it denotes the CJ pattern.

$\theta_1$	$\theta_2$	$\Theta_3, \theta_5$ (°)		$\theta_7, \theta_8$ (°)		$\theta_9, \theta_{10}$ (°)		$\theta_{11}, \theta_{12}$ (°)	
		Theory	Simulation	Theory	Simulation	Theory	Simulation	Theory	Simulation
7.5	12	−23.2	(−23.1, −22.8)	−8.1	(−8.3, −7.8)	...			
	16		(−23.5, −22.8)	−4.2	(−4.5, −3.5)				
	20		(−23.6, −21.2)	−0.7	(−1.0, 1.0)				
	24*	(−24.0, −22.5)	...		−8.8	(−12.5, −10.0)	16.3	(13.1, 14.0)	
	20*	(−25.0, −23.0)					(−13.0, −11.0)	13.1	(5.0, 7.5)
	16*	(−25.0, −23.5)					(−14.0, −12.0)	−0.1	(−2.5, 0)
19	25	−1.5	(−1.3, 0)	22.9	(22.5, 23.0)	...			
	25.5		(−4.8, −3.6)	23.4	(18.8, 21.0)				
	25.5*	(−0.4, 1.8)	...		19.6	(13.3, 15.6)	27.2	(27.3, 29.7)	
	26*	(−1.7, 2.0)					(22.5, 25.6)	28.1	(27.5, 31.2)

The pressure ratios and flow deflection angles obtained by the shock polar analysis are quantitatively compared with those obtained through numerical simulations in Tables I and II, respectively. The numerical results in Tables I and II are given in the form of a parameter range, which is the variation of the pressure ratios and flow deflection angles in a small range across the slip lines at the shock intersection points due to the following reasons. In theory, the shock wave exists as a strong discontinuity surface, after which the flow parameters abruptly change. In contrast, in the numerical simulations, the flow parameters continuously vary. The shock wave is simulated by a sharp but continuous change in the flow parameters over a finite distance. Based on the accuracy of the numerical method and grid resolution, this finite distance could smear several grids. On the other hand, in theory, only the cases where the shock wave is followed by a uniform flow field, i.e., a straight shock wave, are dealt with. For the triple point with the participation of a bow shock wave, the theory predicts the flow parameters in an extremely small region very close to the shock intersection point, where the bow shock wave can be regarded as an oblique shock wave of infinitely small length.

Tables I and II show that for the CJ mode (the cases without superscript \*), the deviation between the theoretical and numerical results is well within the acceptable range, and the pressure ratios obtained from the simulations are generally higher than those theoretically obtained. For the DJ mode, the deviations between the theoretical and numerical results are large, which are mainly concentrated in the regions (9)–(12) [Fig. 2(b)]. The numerically calculated flow deflection angles,  $\theta_9$ – $\theta_{12}$ , are lower than the theoretical values, while the corresponding pressure ratios,  $p_9$ – $p_{12}$ , are higher than the theoretical values. The discrepancies between the theoretical and numerical results may partly stem from the errors introduced by the numerical method, grid resolutions, and observations, but they mainly stem from the strong back pressure afforded by the cylinder downstream and the secondary waves generated by the disturbance introduced by the cylinder. The deviations between the theoretically and numerically obtained flow deflection angle and pressure also lead to the discrepancies of the theoretically and numerically obtained transitional angles.

The deviations between the theoretically and numerically obtained transitional angles are analyzed. The transformation of

**TABLE II.** Comparison of flow deflection angles of different interference regions obtained by shock polar analysis (theory) and numerical calculations (simulation). The case with superscript \* indicates the DJ pattern; otherwise, it denotes the CJ pattern.

$\theta_1$	$\theta_2$	$P_3, p_5$		$p_7, p_8$		$p_9, p_{10}$		$p_{11}, p_{12}$	
		Theory	Simulation	Theory	Simulation	Theory	Simulation	Theory	Simulation
7.5	12	73.7	(74.3, 75.7)	174.4	(176.4, 180)	...			
	16		(76.3, 78.8)	213.4	(215.2, 220)				
	20		(72.0, 78.0)	254.3	(252.2, 259.0)				
	24*	(73.8, 75.0)	...		168.6	(165.0, 172.5)	169.2	(167.0, 171.0)	
	20*	(76.8, 82.4)					(160.0, 172.5)	169.3	(171.7, 176.7)
	16*	(80.0, 82.5)					(168.3, 172.5)	169.2	(170.0, 180.0)
19	25	74.5	(70.0, 72.5)	305.7	(304.0, 308.0)	...			
	25.5		(86.0, 88.0)	312.7	(343.5, 350.0)				
	25.5*	(62.0, 66.0)	...		257.7	(275.0, 300.0)	257.2	(255.0, 267.5)	
	26*	(62.3, 69.7)					(280.0, 300.0)	257.1	(263.3, 271.7)

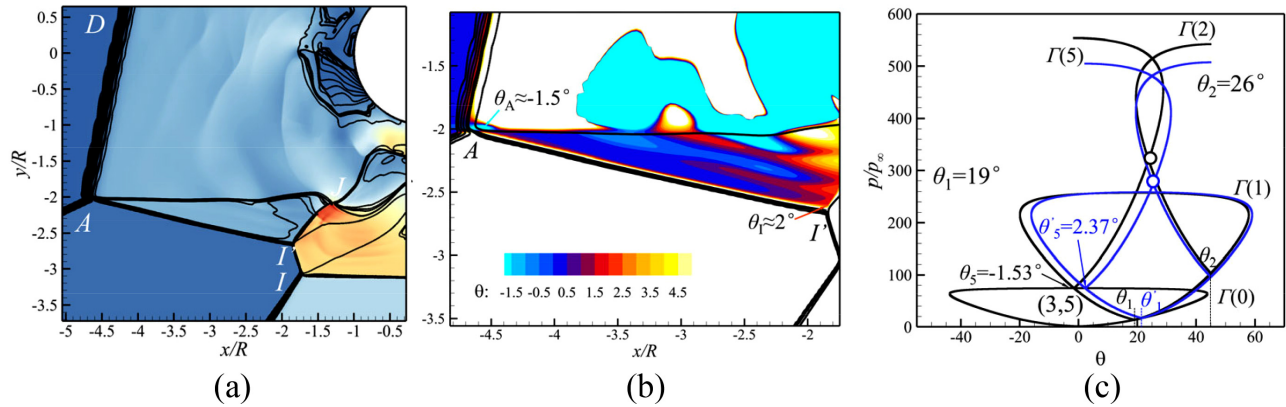


FIG. 12. Numerical results of the dimensionless pressure  $p/p_\infty$  contours for  $M_\infty = 8.0$ ,  $\theta_1 = 19^\circ$ , and  $\theta_2 = 26^\circ$  (a) with an enlarged view of the distributions of the deflection angle  $\theta_5$  near the intersection point I (b), and the shock polar solution in (c).

DJ→CJ is believed to be driven by the curvature of the transmitted shock AI. In the theoretical analysis, AI is assumed to be straight to evaluate the flow parameters at I through those of A. However, in an actual flow, AI is curved due to the influence of secondary waves in the flow field. Figure 12 provides the dimensionless pressure contour of the flow field of  $M_\infty = 8.0$ ,  $\theta_1 = 19^\circ$ , and  $\theta_2 = 26^\circ$  [Fig. 11(c)]; distributions of the flow deflection angle behind AI, that is,  $\theta_5$ ; and the corresponding shock polar solutions. Figure 12(a) shows that the flow in the region AIJ is non-uniform due to the entropy waves generated behind the bow shock segment AD. Figure 12(b) suggests that the deviation of the flow deflection angle between A and I is about  $3.5^\circ$ . Figure 8 shows that the von Neumann condition is significantly elevated as  $\theta_1$  increases, which is equivalent to the increase in  $\theta_5$ . When the  $\theta_1$  value is increased so that the flow deflection angle in region (5) agrees with the numerical results, Fig. 12(c) shows that the intersection of the polar  $\Gamma(5)$  and polar  $\Gamma(2)$  lies very close to the von Neumann condition (see the blue lines). Therefore, the DJ→CJ transition obtained by numerical simulation unsurprisingly occurs at  $\theta_2 = 25.5^\circ$ . The CJ→DJ transition is advanced most likely because of the downstream disturbance. Hu *et al.*<sup>29</sup> determined that the transition of RR→MR was advanced due to the downstream disturbance in the double-wedge configuration. Moreover, the oMR configuration with a diverging subsonic stream tube can be numerically obtained, which is theoretically impossible. In this study, the cylinder acts as a source of strong disturbance downstream, affecting the shock reflection at point I through the subsonic region. The mechanism will be studied in future studies. Further numerical confirmations of the hysteresis for  $\theta_1 > \theta_1^{St}$  can be obtained by appropriately increasing  $M_\infty$  or decreasing  $\theta_1$ , as suggested in Fig. 8.

D. Influence of computation domain

This section investigates the possible reasons for the DJ→CJ transition observed by Hsu and Ijaz.<sup>38</sup> The investigated case corresponds to Run 86 in Wieting’s experiments,<sup>37</sup> wherein  $M_\infty = 8.0$ ,  $\theta_1 = 7.5^\circ$ , and  $\theta_2 = 6^\circ$ . As shown in Fig. 5,  $\theta_2 = 6^\circ$  is well below the line of  $\theta_2^{VN}$ ; thus, the CJ configuration is the only possible steady solution. Figure 13 displays the shock polar solution for this case. The intersection point of polar  $\Gamma(5)$  and polar  $\Gamma(2)$  lies below the strong solution

portion of  $\Gamma(1)$ . This indicates that the pressure increases across the transmitted shock AI’ and I’J’ and that  $K_2$ I’ and BI’ [Fig. 2(b)] cannot be balanced with the pressure across the Mach stem I’J’ without specifying additional boundary conditions. On the other hand, shock polars  $\Gamma(5)$  and  $\Gamma(2)$  intersect with the upper portion of  $\Gamma(1)$  and generate a UuSL and an LdSL, respectively. In this case, a diverging subsonic stream tube forms, which is theoretically unstable. The aforementioned analysis shows that the transition reason speculated by Hsu and Ijaz<sup>38</sup> is partly correct. They stated that the CJ pattern is the only possible quasi-steady-state solution and the DJ pattern is a transient phenomenon. However, our findings suggest that this statement should be limited to the flow field under the same boundary condition of Run 86 and that the flow is clear of disturbances.

During the generation of a bow shock wave, the cylinder is a source of strong disturbance, which can provide the strong back pressure required to stabilize the theoretically unstable DJ [UuSL + LdSL]. Figure 14(a) depicts the numerical results of MSSI with the same

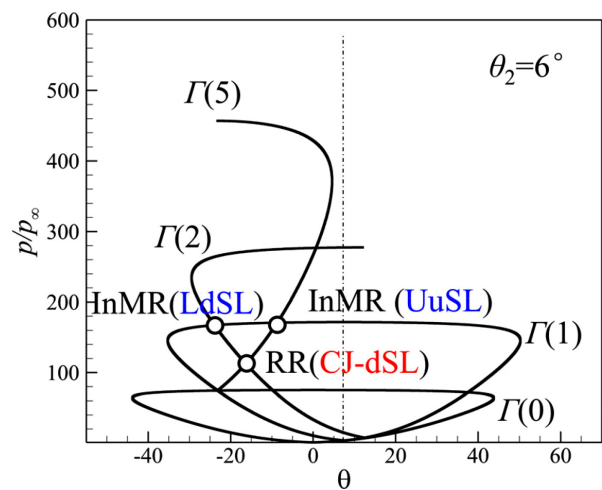
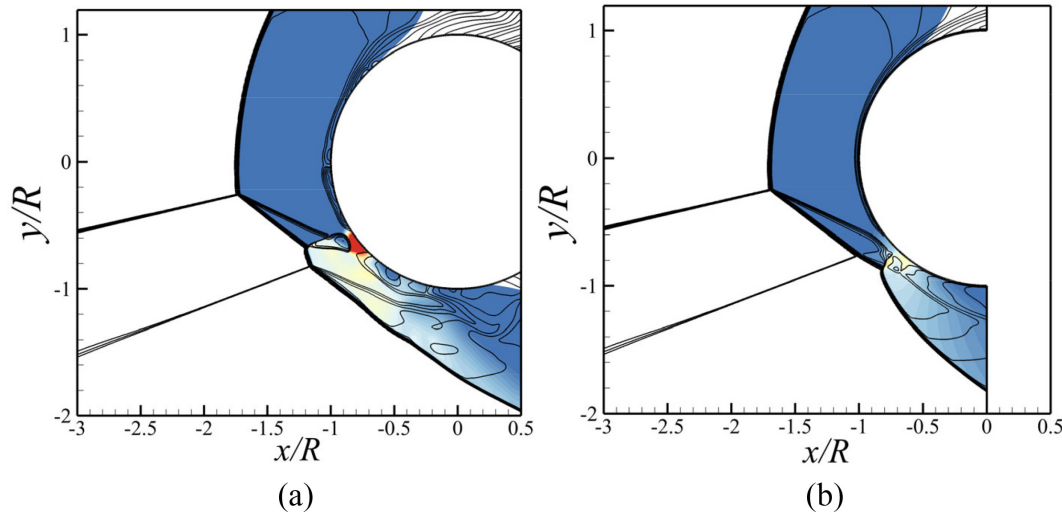


FIG. 13. Diagram of shock polar solution for Run 86 ( $M_\infty = 8.0$ ,  $\theta_1 = 7.5^\circ$ , and  $\theta_2 = 6^\circ$ ).

08 April 2024 03:06:59



**FIG. 14.** Numerical results of flow interference structures calculated based on the (a) present computation domain and (b) the computation domain used by Hsu and Ijaz.<sup>38</sup> The incoming flow parameters are the same as those of Run 86, with a further downward intersection position of the second incident shock wave.

incoming flow as Run 86, but the intersection position of the second incident shock is more downward. As shown in Fig. 14(a), a stable DJ [UuSL + LdSL] forms due to the back pressure provided by the cylinder. The computation domain used in this study [Fig. 9(b)] is different from that used by Hsu and Ijaz<sup>38</sup> [Fig. 9(a)]. The same DJ→CJ transformation occurs [Fig. 14(b)] when using the computation domain shown in Fig. 9(a). This suggests that the transformation of the wave patterns observed by Hsu and Ijaz was likely influenced by the computational domain. The computational domain shown in Fig. 9(a) cannot guarantee that the flow is supersonic at the outlet. When the outlet contains a large subsonic region, the downstream disturbance could propagate upstream and influence the interference structures. Figure 14(b) shows that during the calculation process, the bow shock is pushed ahead until the DJ pattern changes into the CJ pattern and the flow returns to supersonic at the outlet.

#### IV. CONCLUSIONS

This study theoretically and numerically analyzed the transition criterion and hysteresis of MSSI.

The transition criterion for MSSI was proposed based on the reflection configuration at intersection point I of the second incident shock  $K_2I$  and the transmitted shock AI of the first incident shock  $K_1A$ . The sufficient condition for the CJ→DJ transition occurs at the detachment condition  $\theta_2^{Det}(M_0, \theta_1)$ . The necessary condition for the reverse occurs at the von Neumann condition  $\theta_2^{vN}(M_0, \theta_1)$ . The theoretical results showed that the line of  $\theta_2^{Det}(M_0, \theta_1)$  always lies above that of  $\theta_2^{vN}(M_0, \theta_1)$ , indicating the existence of a DSI. The DSI widens when  $M_0$  increases or  $\theta_1$  decreases.

The existence of DSI and the two different sequences of wave patterns analytically predicted were numerically validated. The numerical results showed that both the CJ→DJ and DJ→CJ transitions are advanced compared to the theoretical predictions, resulting in a narrower DSI. Comparison of the flow deflection angles and pressure ratios obtained from the numerical simulations and theoretical analysis showed that the numerically obtained pressure ratios were higher

than those theoretically obtained. The reasons for the advancement of both transitions were analyzed. The CJ→DJ transition is advanced due to the strong back pressure imposed by the cylinder, which leads to the persistence of the DJ mode beyond its theoretical value. Furthermore, the DJ→CJ transition is advanced because of secondary waves in the flow field, which increases the actual flow deflection angle in region (5). The results showed that the effect of the secondary waves significantly increases with  $\theta_1$ .

In addition, the possible reasons for the DJ→CJ transformation observed by Hsu and Ijaz<sup>38</sup> were analyzed. The results showed that the transformation likely occurs due to the effect of the computational domain. When the outlet of the computational domain does not guarantee the supersonic conditions, the perturbation propagates upstream through the subsonic region and pushes the transmitted shock wave forward until the DJ→CJ transition occurs. Moreover, the theoretically impermissible DJ [UuSL + LdSL] configuration can be stabilized by the strong back pressure provided by the cylinder.

Subsequently, the transition criterion for MSSI was explicitly proposed for the first time, and the existence of hysteresis was theoretically and numerically verified. Additional flow characteristics of MSSI were elaborated by numerical simulations. These results are essential when multiple compression shock waves fail to converge at the inlet lip, which should be accounted for in the design of hypervelocity intakes.

As an initial study on the MSSI phenomenon, the gas model considered in this study is quite a simplified gas model, the perfect gas model, and does not consider the real gas effect and viscosity. The real gas effect mainly affects the thermodynamic parameters of the flow behind the strong shock waves, i.e., the flow behind the bow shock wave and the Mach stem. In the considered Mach number range, the real gas effect is mainly manifested by the vibration energy excitation of gas molecules, the decrease in the specific heat ratio, and the decrease in the stand-off distance of shock waves. Consequently, the length of the Mach stem decreases, advancing the CJ→DJ transition and delaying the DJ→CJ transition, which results in the widening of

the hysteresis interval. Viscosity mainly affects the shear layer and not the boundary layer as the boundary layer of the cylinder surface is poorly developed in such flow fields. The gas viscosity promotes the dissipation of the shear layer and suppresses its instability. Therefore, when the flow viscosity is considered, the scale and number of the vortices formed by the destabilization and shedding of the shear layer will be suppressed. The effect of viscosity on the interference configurations and its hysteresis needs to be studied as its effect on the shear layer needs to be considered in conjunction with the impingement position and the intrinsic oscillatory characteristics of the jets, which is a complex topic.

## ACKNOWLEDGMENTS

This work was supported by the National Key Research and Development Plan of China under Grant No. 2019YFA0405204 and the National Natural Science Foundation of China under Grant Nos. 12172365, 12072353, and 12132017.

## AUTHOR DECLARATIONS

### Conflict of Interest

The authors have no conflicts to disclose.

### Author Contributions

**Mingyue Lin:** Writing – original draft (lead). **Fan Yang:** Data curation (equal). **Zongmin Hu:** Project administration (lead); Writing – original draft (equal). **Chun Wang:** Funding acquisition (equal). **Zonglin Jiang:** Conceptualization (equal); Funding acquisition (equal).

## DATA AVAILABILITY

The data that support the findings of this study are available from the corresponding author upon reasonable request.

## REFERENCES

- Y.-C. Hu, W.-F. Zhou, G. Wang, Y.-G. Yang, and Z.-G. Tang, “Bistable states and separation hysteresis in curved compression ramp flows,” *Phys. Fluids* **32**, 113601 (2020).
- E. Mach, “Über den verlauf von funkenwellen in der ebene und im raume,” *Sitzungsber. Akad. Wiss. Wien* **78**, 819 (1878).
- J. Neumann, “Refraction, intersection and reflection of shock waves,” NAVROD Report No. 203-245 (Navy Department Bureau of Ordinance, Washington DC, USA, 1945).
- H. G. Hornung, H. Oertel, and R. J. Sandeman, “Transition to Mach reflexion of shock waves in steady and pseudosteady flow with and without relaxation,” *J. Fluid Mech.* **90**, 541 (1979).
- L. F. Henderson and A. Lozzi, “Further experiments on transition to Mach reflexion,” *J. Fluid Mech.* **94**, 541 (1979).
- H. G. Hornung and M. L. Robinson, “Transition from regular to Mach reflection of shock waves—Part 2: The steady-flow criterion,” *J. Fluid Mech.* **123**, 155 (1982).
- A. Chpoun, D. Passerel, H. Li, and G. Ben-Dor, “Reconsideration of oblique shock wave reflections in steady flows—Part I: Experimental investigation,” *J. Fluid Mech.* **301**, 19 (1995).
- J. Vuillon, “Reconsideration of oblique shock wave reflections in steady flows—Part II: Numerical investigation,” *J. Fluid Mech.* **301**, 37 (1995).
- G. Ben-Dora, M. Ivanovb, E. I. Vasiliev, and T. Elperina, “Hysteresis processes in the regular reflection Mach reflection transition in steady flows,” *Prog. Aerosp. Sci.* **38**, 347 (2002).
- H. G. Hornung and M. Robinson, “Transition from regular to Mach reflection of shock waves Part 2: The steady-flow criterion,” *J. Fluid Mech.* **123**, 155–164 (1982).
- Q. Wang, F. Qu, Q. Zhao, and J. Bai, “Numerical study of the hysteresis effect on the supersonic airfoil for the transonic circulation control,” *Aerosp. Sci. Technol.* **126**, 107645 (2022).
- Z. Li, P. Zhang, D. Yang, and J. Zhang, “Numerical investigations on the key contributing factor and flow features of compressor stall hysteresis,” *Aerosp. Sci. Technol.* **121**, 107306 (2022).
- Y. Jin, S. Sun, H. Tan, Y. Zhang, and H. Huang, “Flow response hysteresis of throat regulation process of a two-dimensional mixed-compression supersonic inlet,” *Chin. J. Aeronaut.* **35**, 112 (2022).
- D. Wang and Y. Yu, “Shock wave configurations and reflection hysteresis outside a planar Laval nozzle,” *Chin. J. Aeronaut.* **28**, 1362 (2015).
- S. M. Boldyrev, V. Y. Borovoy, A. Y. Chinilov, V. N. Gusev, S. N. Krutiy, I. V. Struminskaya, L. V. Yakovleva, J. Delery, and B. Chanetz, “A thorough experimental investigation of shock/shock interferences in high Mach number flows,” *Aerosp. Sci. Technol.* **5**, 167 (2001).
- C.-Y. Bai and Z.-N. Wu, “Type IV shock interaction with a two-branch structured transonic jet,” *J. Fluid Mech.* **941**, A45 (2022).
- A. Khatta and J. Gopalan, “Hypersonic shock tunnel studies of Edney Type III and IV shock interactions,” *Aerosp. Sci. Technol.* **72**, 335 (2018).
- D. Das, S. Desai, V. Kulkarni, and H. Gadgil, “Real-gas effects for shock/shock interaction in Earth and Mars atmospheres,” *J. Spacecr. Rockets* **59**, 1853 (2022).
- M. J. Frame and M. J. Lewis, “Analytical solution of the type IV shock interaction,” *J. Propul. Power* **13**, 601 (1997).
- B. Edney, “Anomalous heat transfer and pressure distributions on blunt bodies at hypersonic speeds in the presence of an impinging shock,” Report No. FFA-115, 1968.
- C. Windisch, B. U. Reinartz, and S. Müller, “Investigation of unsteady Edney Type IV and VII shock–shock interactions,” *AIAA J.* **54**, 1846 (2016).
- Z. M. Hu, R. S. Myong, C. Wang, T. H. Cho, and Z. L. Jiang, “Numerical study of the oscillations induced by shock/shock interaction in hypersonic double-wedge flows,” *Shock Waves* **18**, 41 (2008).
- A. S. Durna, M. E. A. Barada, and B. Celik, “Shock interaction mechanisms on a double wedge at Mach 7,” *Phys. Fluids* **28**, 096101 (2016).
- Z. M. Hu, R. S. Myong, Y. R. Yang, and T. H. Cho, “Reconsideration of inviscid shock interactions and transition phenomena on double-wedge geometries in a M-infinity = 9 hypersonic flow,” *Theor. Comput. Fluid Dyn.* **24**, 551 (2010).
- J. Hao and C.-Y. Wen, “Hypersonic flow over spherically blunted double cones,” *J. Fluid Mech.* **896**, A26 (2020).
- B. Q. Meng, G. L. Han, C. K. Yuan, C. Wang, and Z. L. Jiang, “Experimental and numerical study on hypersonic flow over double-wedge configuration,” *AIAA J.* **55**, 3227 (2017).
- J. Olejniczak, M. J. Wright, and G. V. Candler, “Numerical study of inviscid shock interactions on double-wedge geometries,” *J. Fluid Mech.* **352**, 1–25 (1997).
- Z. M. Hu, C. Wang, Y. Zhang, and R. S. Myong, “Computational confirmation of an abnormal Mach reflection wave configuration,” *Phys. Fluids* **21**, 011702 (2009).
- Z. M. Hu, Y. L. Gao, R. S. Myong, H. S. Dou, and B. C. Khoo, “Geometric criterion for RR→MR transition in hypersonic double-wedge flows,” *Phys. Fluids* **22**, 016101 (2010).
- W. Xiong, J. Li, Y. Zhu, and X. Luo, “RR–MR transition of a Type V shock interaction in inviscid double-wedge flow with high-temperature gas effects,” *Shock Waves* **28**, 751 (2018).
- J. Hao, C.-Y. Wen, and J. Wang, “Numerical investigation of hypervelocity shock-wave/boundary-layer interactions over a double-wedge configuration,” *Int. J. Heat Mass Transfer* **138**, 277 (2019).
- J. Li, Y. Zhu, and X. Luo, “On Type VI–V transition in hypersonic double-wedge flows with thermo-chemical non-equilibrium effects,” *Phys. Fluids* **26**, 086104 (2014).
- W. Xiong, Y. Zhu, and X. Luo, “On transition of type V interaction in double-wedge flow with non-equilibrium effects,” *Theor. Appl. Mech. Lett.* **6**, 282 (2016).
- X.-K. Guan, C.-Y. Bai, J. Lin, and Z.-N. Wu, “Mach reflection promoted by an upstream shock wave,” *J. Fluid Mech.* **903**, A44 (2020).
- X.-K. Guan, C.-Y. Bai, and Z.-N. Wu, “Steady Mach reflection with two incident shock waves,” *J. Fluid Mech.* **855**, 882 (2018).
- X.-K. Guan, C.-Y. Bai, and Z.-N. Wu, “Double solution and influence of secondary waves on transition criteria for shock interference in pre-Mach reflection with two incident shock waves,” *J. Fluid Mech.* **887**, A22 (2020).

- <sup>37</sup>A. Wieting, "Multiple shock-shock interference on a cylindrical leading edge," *AIAA J.* **30**, 2073 (1992).
- <sup>38</sup>K. Hsu and H. Ijaz, "Simulation of multiple shock-shock interference patterns on a cylindrical leading edge," *AIAA J.* **34**, 764 (1996).
- <sup>39</sup>Z. Jiang, J. Li, J. W. Z. Lu, A. Y. T. Leung, V. P. Iu, and K. M. Mok, "Heat transfer problems induced by multi-shocks interaction," *AIP Conf. Proc.* **1233**, 987 (2010).
- <sup>40</sup>T.-J. Hsieh, C.-H. Wang, and J.-Y. Yang, "Simulation of multiple shock-shock interference using implicit anti-diffusive WENO schemes," *Int. J. Numer. Methods Fluids* **62**, 138 (2009).
- <sup>41</sup>J. Peng, C. T. Luo, Z. J. Han, Z. M. Hu, G. L. Han, and Z. L. Jiang, "Parameter-correlation study on shock-shock interaction using a machine learning method," *Aerosp. Sci. Technol.* **107**, 106247 (2020).
- <sup>42</sup>J. Peng, S. Li, F. Yang, M. Lin, G. Han, and Z. Hu, "Transitional wave configurations between Type III and Type IV oblique-shock/bow-shock interactions," *Chin. J. Aeronaut.* **36**, 96 (2023).
- <sup>43</sup>Z. Zhang, C. Wen, W. Zhang, Y. Liu, and Z. Jiang, "Formation of stabilized oblique detonation waves in a combustor," *Combust. Flame* **223**, 423 (2021).
- <sup>44</sup>H. Lu, L. Yue, Y. Xiao, and X. Zhang, "Interaction of isentropic compression waves with a bow shock," *AIAA J.* **51**, 2474 (2013).